Journal of Scientific Computing (2025) 105:42
https://doi.org/10.1007/s10915-025-03070-1

Multidomain Fourier-Chebyshev Spectral Method for Computing Rogue waves in the Nonlinear Schrödinger Equation

Sheng Chen[1] · Guangshen Liu[2,5] · Zhiguo Xu[3] · Yong Zhang[4]

Received: 31 March 2025 / Revised: 25 July 2025 / Accepted: 12 September 2025 /
Published online: 25 September 2025

Abstract
In this article, we propose a time-splitting multidomain Fourier-Chebyshev spectral method to compute rogue wave solutions to the two-dimensional nonlinear Schrödinger equation in the whole space, which usually decay very slowly at the far field. To approximate the slow-decay function over the whole space, we first expand the wave function with Fourier basis in the azimuthal direction, then propose the C^1-continuity multidomain Chebyshev spectral method in the radial direction. Our scheme is second order in time and spectrally accurate in space. Extensive numerical results, together with theoretical analysis, are presented to confirm the efficiency and accuracy for wave functions with different decay rates. In addition, the successful simulation of rogue wave further validates our method.

Keywords rogue wave · 2D nonlinear Schrödinger equation · whole space · slow-decay · multidomain Fourier-Chebyshev spectral method

✉ Yong Zhang
Zhang_Yong@tju.edu.cn

Sheng Chen
shengchen@bnu.edu.cn

Guangshen Liu
guangshen.liu@connect.polyu.hk

Zhiguo Xu
xuzg2014@jlu.edu.cn

1 Research Center for Mathematics, Beijing Normal University, Zhuhai, China

2 Department of Applied Mathematics, The Hong Kong Polytechnic University, Hong Kong, China

3 School of Mathematics, Jilin University, Changchun, China

4 Center for Applied Mathematics and KL-AAGDM, Tianjin University, Tianjin, China

5 School of Mathematical ScienceEastern, Institute of Technology, Ningbo, China

Contents

1 Introduction

Rogue waves, initially defined as extremely high waves suddenly appearing in the ocean [23], has become widely accepted to describe isolated, large-amplitude waves in various fields [24], including the optics [2, 28], superfluids [12], Bose-Einstein condensates [21], and finance [35]. In order to detect and predict this unexpected phenomenon, for years, researchers delve into the physical mechanisms behind [20]. It is very important to gain some insights, either theoretically or numerically, so to predict or even control such physics. A specific mechanism is identified based on the Modulational instability [22]. In this article, we embark on a popular model [20], the nonlinear Schrödinger equation (NLSE), to study the phenomenon of rogue wave (RW):

$$\begin{cases} i\,\partial_t \psi(\mathbf{x}, t) = \Big[-\Delta + \mathcal{N}(|\psi(\mathbf{x}, t)|^2, \mathbf{x}) \Big] \psi(\mathbf{x}, t), \quad \mathbf{x} \in \mathbb{R}^2, \quad t > 0, \\ \psi(\mathbf{x}, 0) = \psi_0(\mathbf{x}), \quad \mathbf{x} \in \mathbb{R}^2, \end{cases} \tag{1.1}$$

where the initial function $\psi_0(\mathbf{x})$ decays to zero at the far field, i.e., $\lim_{|\mathbf{x}|\to\infty} \psi_0(\mathbf{x}) = 0$. The decay properties can critically influence the dynamics. The formation of rogue waves like the Peregrine soliton [25] and its higher-order counterparts [1] is often attributed to the slow-decay initial profiles. This slow-decay behavior is preserved durning evolution [9, 11]. Therefore, we are motivated to study the following slow-decay problem:

$$\psi(\mathbf{x}, t) \to \frac{A(t)}{(1 + |\mathbf{x}|)^p}, \quad |\mathbf{x}| \to \infty, \quad t \geq 0, \tag{1.2}$$

where $p \in \mathbb{R}^+$ is the decay rate and $A(t)$ is a complex-valued function. While a canonical choice for the nonlinear term in rogue wave simulations is the following cubic nonlinearity [25, 32]

$$\mathcal{N}(|\psi(\mathbf{x}, t)|^2, \mathbf{x}) = \pm 2|\psi(\mathbf{x}, t)|^2, \tag{1.3}$$

our numerical simulation will explore various nonlinearities to demonstrate the performance.

As is known, it is difficult to find exact solutions to the above NLSE, therefore, we need to resort to numerical simulation. Recently, there has been a growing interest in the RW simulation [19, 33], however, as far as we know, there are quite few studies on efficient numerical methods. This can be attributed to the fact that the wave function may decay very slowly at

the far field, for example, it may decay with a polynomial or fractional rate as show above in (1.2). To numerical capture such whole space function is some challenging, especially for slow-decay function, and it usually requires either some intricate *a priori* information for truncation to bounded domain or a suitable whole space numerical method, which of course often leads to a larger, sometimes even prohibitively huge, complexity. Therefore, to develop an efficient and accurate simulation method is very intricate, and requires one to strike a balance between accuracy, efficiency and numerical instability, sometimes, especially when the long term simulation is inevitable.

Fortunately, as demonstrated by Bao et al. [4], after applying the time splitting method in the temporal direction, the main difficulty lies in efficient computation of the whole space linear subproblem

$$i\,\partial_t \psi(\mathbf{x}, t) = -\Delta \psi(\mathbf{x}, t), \quad \mathbf{x} \in \mathbb{R}^2, \tag{1.4}$$

while the remaining nonlinear subproblem can be integrated analytically in physical space.

To solve the above unbounded problem, one common approach is to first truncate the whole space into bounded domain and then impose appropriate boundary conditions. The approximation of boundary conditions is of essential importance and sometimes bottlenecks the simulation in terms of accuracy and efficiency. For the fast-decay case, various effective methods have been proposed [26]. Since the wave function decays very rapidly at the far field, the whole space problem is usually truncated on a bounded domain and imposed with simple boundary conditions, such as homogeneous Dirichlet and periodic boundary conditions [7, 34]. For example, Wang designed an efficient Chebyshev-Tau method for Ginzburg–Landau–Schrödinger equation [30]. Recently, Zhang et al. proposed a Chebyshev-Fourier spectral method to compute dynamics of a two-dimensional rotating dipolar Bose-Einstein condensation in polar coordinates [31]. While, for the slow-decay or even nonzero limit case, it is not appropriate to impose simple boundary conditions as those for the fast-decay case. We shall design appropriate boundary conditions using *a priori* information or estimates if available, and the boundary conditions often vary case by case. For example, Bao et al. designed accurate and simple artificial boundary conditions for computing the dynamics of solitons [5]. To capture the nonzero background and algebraic decay at the far field, Wang et al. introduced high order boundary conditions based on far-field asymptotic expansions for rational polynomial solutions [32]. We refer the readers to [3] for a comprehensive review on boundary condition techniques for Schrödinger equations.

Instead of solving a bounded domain problem with boundary conditions, another effective approach is to solve the equation directly on the whole space. One popular approach is to utilize classical orthogonal functions on unbounded domain [10]. It has been verified that the classical Hermite or composite Laguerre-Legendre spectral methods are successful in handling exponential-decay solutions [13, 14, 17, 18]. However, these traditional spectral methods are inefficient for slow-decay functions. To tackle this problem, researchers turn to mapped orthogonal functions, e.g., mapped Jacobi polynomial [27], and have developed corresponding approximation theories. For example, Guo et al. developed the mapped Chebyshev & Legendre functions using rational mappings [15, 16]. Such rational functions have manifested excellent performance in approximating algebraic-decay functions, and we refer to [27] for details. Unfortunately, rational functions are not as effective for slow fractional-decay functions. Therefore, it is imperative to develop appropriate methods to approximate the fractional-decay functions.

In this article, we first expand the wave function ψ with Fourier basis in the azimuthal direction. The original two-dimensional problem (1.4) is then decomposed into a series of

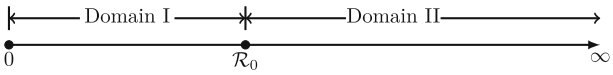

Fig. 1 Bi-partition of the half line $\mathbb{R}^+$

ordinary differential problems as follows

$$i\partial_t \varphi_k(r,t) = \left[-\frac{\partial^2}{\partial r^2} + \frac{1}{r}\frac{\partial}{\partial r} - \frac{k^2}{r^2} \right] \varphi_k(r,t), \quad r \in (0,\infty), \tag{1.5}$$

where $\varphi_k(r,t)$ is the Fourier mode given explicitly

$$\varphi_k(r,t) = \frac{1}{2\pi}\int_0^{2\pi} \varphi(r,\theta,t) e^{-ik\theta} \mathrm{d}\theta, \quad k \in \mathbb{Z}. \tag{1.6}$$

Note that the wave function may exhibit either fast exponential-decay or slow polynomial-decay at the far field. It is no doubt that an effective method should work for both fast and slow decay cases. In order to enhance the spatial resolution, we draw inspiration from the ideas presented in [6] and propose a multidomain spectral method. Specifically, we split the half line $\mathbb{R}^+$ into two parts, referred to as $\mathcal{D}_1 = (0, \mathcal{R}_0]$ and $\mathcal{D}_2 = [\mathcal{R}_0, +\infty)$ with $\mathcal{R}_0 > 0$ being the junction point, and leverage piecewise Chebyshev and mapped Chebshev interpolation to approximate the Fourier mode $\varphi_k(r,t)$ in radial direction respectively.1

With such multidomain method, the Fourier mode $\varphi_k(r)$ is usually enforced with C^0-continuity matching conditions at the junction point $\mathcal{R}_0$. Then we apply the Chebyshev spectral method in each domain to guarantee the matching conditions hold true. Unfortunately, the fully discrete system of (1.5) suffers from poor numerical stability, leading to a significant accuracy loss. Therefore, we delve into the optimal continuity order of matching conditions, and find that the C^1-continuity conditions admits a better stability and is quite easy to implement. Furthermore, we employ a high-order mapping [8] and propose a spectral accurate method that works for both fast exponential-decay and slow fractional-decay problems.

The paper is organized as follows. In Section 2, we utilize time-splitting method and Fourier spectral method to decompose the two-dimensional nonlinear Schrödinger equation (NLSE) into a series of time-dependent half-line ordinary differential equations. Then we proposed the C^1-continuity multidomain Chebyshev spectral method (MCSM) in Section 3 where the C^1-continuity matching conditions are utilized to ensure smoothness. Moreover, we introduce a high order mapping to deal with slow-decay solution. In Section 4, we present extensive numerical results to confirm the accuracy and efficiency. Some conclusions are drawn in Section 5, supplemented by related theorems provided in Appendix Appendix A.

2 Computational Dimension Reduction

In this section, we will apply the time-splitting method and Fourier spectral decomposition to streamline the problem into a series of radial components. The following parts will delve into the practical application of the time-splitting method in conjunction with Fourier spectral decomposition, shedding light on how these methodologies synergize to simplify the nonlinear Schrödinger equation (NLSE), particularly transforming into a set of radial components.

2.1 Time Splitting Method

As demonstrated in Bao et al. [4], it is known that the original nonlinear Schrödinger equation (NLSE) can be approximated by combining

$$i\,\partial_t \psi(\mathbf{x}, t) = -\Delta \psi(\mathbf{x}, t), \tag{2.7}$$

and

$$i\,\partial_t \psi(\mathbf{x}, t) = \mathcal{N}(|\psi(\mathbf{x}, t)|^2, \mathbf{x})\psi(\mathbf{x}, t), \tag{2.8}$$

where one has already proved that the nonlinear term $\mathcal{N}(|\psi(\mathbf{x}, t)|^2, \mathbf{x})$ is invariant of time t. Hence, for any $t \in [t_n, t_{n+1}]$, the solution of equation (2.8) can be drived that

$$\psi(\mathbf{x}, t) = e^{-i\mathcal{N}(|\psi^n(\mathbf{x})|^2, \mathbf{x})(t-t_n)}\psi^n(\mathbf{x}), \quad t \in [t_n, t_{n+1}],$$

with $\psi^n(\mathbf{x}) = \psi(\mathbf{x}, t_n)$. Let τ be the constant time step and $t_n = n\tau$. We can solve the NLSE, evolving (1.1) from t_n to t_{n+1}, by the second-order Strang splitting method [4] as follows:

- Update the known data $\psi^n(\mathbf{x}) = \psi(\mathbf{x}, t_n)$ with the half-time step $\tau/2$ via

$$\psi^{(1)}(\mathbf{x}) = e^{-i\mathcal{N}(|\psi^n(\mathbf{x})|^2, \mathbf{x})\tau/2}\psi^n(\mathbf{x}). \tag{2.9}$$

- Solve the following free Schrödinger equation with a suitable temporal scheme:

$$\begin{cases} i\,\partial_t \psi(\mathbf{x}, t) = -\Delta \psi(\mathbf{x}, t), \quad \mathbf{x} \in \mathbb{R}^2, \quad t \in [t_n, t_{n+1}], \\ \psi(\mathbf{x}, t_n) = \psi^{(1)}(\mathbf{x}), \quad \mathbf{x} \in \mathbb{R}^2. \end{cases} \tag{2.10}$$

  and denote the corresponding solution at $t = t_{n+1}$ by $\psi^{(2)}(\mathbf{x})$.
- Evolve (2.8) for half-time step $\tau/2$ with the solution $\psi^{(2)}(\mathbf{x})$ again:

$$\psi^{n+1}(\mathbf{x}) = e^{-i\mathcal{N}(|\psi^{(2)}(\mathbf{x})|^2, \mathbf{x})\tau/2}\psi^{(2)}(\mathbf{x}). \tag{2.11}$$

It is worth mentioning that following the aforementioned linearization process, the subsequent task requires one to develop an accurate, efficient and stable numerical algorithm to solve the free Schrödinger equation (2.10), especially when the long term simulation is inevitable. To this end, a fast algorithm based on Fourier spectral decomposition will be utilized.

2.2 Fourier Decomposition

By employing the Fourier decomposition technique, the problem can be simplified into a set of radial problems. To be specific, we rewrite equation (2.10) in the polar coordinates as

$$\begin{cases} i\,\partial_t \varphi(r, \theta, t) = -(\frac{\partial^2}{\partial r^2} + \frac{1}{r}\frac{\partial}{\partial r} + \frac{1}{r^2}\frac{\partial^2}{\partial \theta^2})\,\varphi(r, \theta, t), \quad t \in [t_n, t_{n+1}], \\ \varphi(r, \theta, t = t_n) = \varphi^n(r, \theta), \quad (r, \theta) \in (0, \infty) \times [0, 2\pi]. \end{cases} \tag{2.12}$$

The wave function $\varphi(r, \theta, t)$ can be approximated by a truncated Fourier series as

$$\varphi(r, \theta, t) \approx \sum_{k=-M/2}^{M/2-1} \varphi_k(r, t)e^{ik\theta}, \quad M \in 2\mathbb{Z}^+, \tag{2.13}$$

where the Fourier mode $\varphi_k(r,t)$, defined as follows,

$$\varphi_k(r,t) = \frac{1}{2\pi}\int_0^{2\pi} \varphi(r,\theta,t)e^{-ik\theta}\mathrm{d}\theta, \tag{2.14}$$

is well approximated by a trapezoidal rule achieving spectral accuracy and the resulted discrete summation is accelerated by discrete Fast Fourier Transform (FFT) [26].

Upon substituting (2.13) into (2.12), the original whole space free Schrödinger equation is transformed into a series of ordinary differential equations, that are defined on half-line of the radial axis, as follows

$$\begin{cases} i\partial_t\varphi_k(r,t) = -\mathcal{L}_k\varphi_k(r,t), \quad t\in[t_n,t_{n+1}], \\ \varphi_k(r,t_n) = \frac{1}{2\pi}\int_0^{2\pi}\varphi(r,\theta,t_n)e^{-ik\theta}\mathrm{d}\theta, \quad r\in(0,\infty), \end{cases} \tag{2.15}$$

with

$$\mathcal{L}_k = \frac{\partial^2}{\partial r^2} + \frac{1}{r}\frac{\partial}{\partial r} - \frac{k^2}{r^2}, \quad k = -M/2, ..., M/2-1. \tag{2.16}$$

The above equation can be discretized in the temporal direction by a Crank-Nicolson scheme achieving a second order accuracy, and the corresponding semi-discrete scheme reads as

$$(\mathcal{I} - \frac{i\tau}{2}\mathcal{L}_k)\varphi_k(r,t_{n+1}) = (\mathcal{I} + \frac{i\tau}{2}\mathcal{L}_k)\varphi_k(r,t_n), \quad r\in(0,\infty), \tag{2.17}$$

where $\mathcal{I}$ is the identity operator and $\varphi_k(r,t_n)$ is the Fourier mode at time t_n. High order schemes can be constructed similarly.

3 C^1-continuity Multidomain Chebyshev Spectral Method

In this section, we shall discuss the spatial discretization and design appropriate numerical algorithm. To this end, we propose the C^1-continuity multidomain Chebyshev spectral method (MCSM) to address the problem stated in (2.17).

3.1 C^0-continuity Multidomain Chebyshev Interpolation

For enhanced comprehension and a self-contained presentation, we start with Chebyshev-Radau polynomial interpolation. For convenience, we adopt the Chebyshev-Gauss-Radau (CGR) points over $[-1,1]$ as follows

$$x_j = \cos\left(\frac{2j+1}{2N+1}\pi\right), \quad j = 0,1,...,N, \tag{3.18}$$

with $-1 = x_N < x_{N-1} < \cdots < x_0 < 1$. The associated Lagrange interpolation polynomial reads as

$$(I_N f)(x) = \sum_{j=0}^{N} f(x_j)\, l_j(x), \quad l_j(x) = \frac{\prod_{k\neq j}(x-x_k)}{\prod_{k\neq j}(x_j-x_k)}, \quad j = 0,\ldots,N, \tag{3.19}$$

and it satisfies the interpolation condition, i.e., $(I_N f)(x_j) = f(x_j)$, $j = 0,1,\ldots,N$. One can approximate the derivative of $f(x)$ by differentiating its interpolation polynomial, that

is, $f' \approx I_N'(f)$ where the prime notation $'$ indicates the derivative was taken with respect to variable x. For CGR points, we have

$$f'(x_k) \approx (I_N f)'(x_k) = \sum_{j=0}^{N} f(x_j)\, l_j'(x_k), \tag{3.20}$$

where $l_j'(x_k)$ can be obtained explicitly and we refer to [26] for more details.

To approximate a continuous function $\varphi(r)$ that is defined on the half-line, we first split the half-line $\mathbb{R}^+$ at the junction point R_0 into two parts as

$$(0, \infty) = (0, \mathcal{R}_0] \cup [\mathcal{R}_0, \infty) := \mathcal{D}_1 \cup \mathcal{D}_2, \tag{3.21}$$

where the finite and infinite interval are denoted by $\mathcal{D}_1$ and $\mathcal{D}_2$ respectively, then we leverage the Lagrange polynomial to approximate $\varphi(r)$ on each interval. Specifically, on interval $\mathcal{D}_1 = (0, \mathcal{R}_0]$, we first introduce a linear change of variables as follows

$$\boxed{r = r_1(x) := \frac{\mathcal{R}_0}{2}\,(1 - x),} \tag{3.22}$$

which maps interval $\mathcal{D}_1$ to the standard interval $[-1, 1]$ of variable x and the CGR points to $0 < r_1(x_0) < r_1(x_1) < \cdots < r_1(x_{N-1}) < r(x_N) = \mathcal{R}_0$, then approximate $\varphi(r)$ by the Lagrange interpolation polynomial of $\varphi(r_1(x))$ at CGR points (3.18) as follows

$$\varphi(r) \approx I_N \varphi(r_1(x)) = \sum_{j=0}^{N} \varphi\big(r_1(x_j)\big)\, l_j(x). \tag{3.23}$$

On infinite interval $\mathcal{D}_2 = [\mathcal{R}_0, \infty)$, using the following nonlinear change of variables

$$\boxed{r = r_2(x) := \frac{2\mathcal{R}_0}{(1 - x)},} \tag{3.24}$$

we map domain $\mathcal{D}_2$ to the standard interval $[-1, 1]$ and the CGR points of x to $\mathcal{R}_0 = r_2(x_N) < r_2(x_{N-1}) < \cdots < r_2(x_1) < r_2(x_0)$ with $r_2(x_0) \to \infty$ as $N \to \infty$, then approximate $\varphi(r)$ by the Lagrange interpolation polynomial of $\varphi(r_2(x))$ at CGR points (3.18) as follows

$$\varphi(r) \approx I_N \varphi(r_2(x)) = \sum_{j=0}^{N} \varphi\big(r_2(x_j)\big)\, l_j(x). \tag{3.25}$$

Therefore, we obtain one C^0 piecewise interpolation polynomial $I_{\mathbf{N}}(r) = I_{(N,N)}(r)$ as

$$I_{\mathbf{N}}\{\varphi\}(r) = \begin{cases} I_N \varphi\big(r_1(x)\big) & r \in \mathcal{D}_1, \\ I_N \varphi\big(r_2(x)\big), & r \in \mathcal{D}_2, \end{cases} \tag{3.26}$$

and it satisfies the C^0-continuity matching condition

$$I_{\mathbf{N}}\{\varphi\}(\mathcal{R}_0 + 0) = I_{\mathbf{N}}\{\varphi\}(\mathcal{R}_0 - 0).$$

Using the error estimates of the classical Chebyshev-Radau interpolation as shown in [26, Theorem 3.42], we derive the error estimates for C^0-continuity multidomain Chebyshev interpolation in Theorem 1.

Theorem 1 *Given a continuous function $\varphi(r)$, $r \in (0, +\infty)$. Denote by $r_1(x) = \mathcal{R}_0(1-x)/2$ and $r_2(x) = 2\mathcal{R}_0/(1-x)$. If $\varphi(r_1(x)), \varphi(r_2(x)) \in B^m_{-\frac{1}{2},-\frac{1}{2}}([-1,1])$, then*

$$\|\varphi - I_{\mathbf{N}}\{\varphi\}\|_w \lesssim N^{-m}, \tag{3.27}$$

where $B^m_{-\frac{1}{2},-\frac{1}{2}}([-1,1])$ is the weighted Sobolev space [26] and $\|\cdot\|_\omega$ represents the weighted L_2 norm with weight function

$$\omega(r) = \begin{cases} r^{-\frac{1}{2}}(\mathcal{R}_0 - r)^{-\frac{1}{2}}, & r \in (0, \mathcal{R}_0], \\ r^{-1}(r - \mathcal{R}_0)^{-\frac{1}{2}}, & r \in [\mathcal{R}_0, +\infty). \end{cases} \tag{3.28}$$

Proof The error estimate is a straightforward result by utilizing the chain rule and the classical results of Chebyshev-Radau interpolation [26]. □

It is important to remark that C^0 piecewise interpolation polynomial is sufficient in terms of approximation accuracy. Nonetheless, to improve numerical stability for solving the radial problems (2.17), a higher continuity matching condition needs to be enforced at junction point $\mathcal{R}_0$. Hence, we introduce the following C^1-continuity multidomain Chebyshev approximation method.

3.2 C^1-continuity Multidomain Chebyshev Approximation

In order to ensure the C^1-continuity at the junction point $\mathcal{R}_0$, we shall first define C^0-continuity piecewise Chebyshev interpolation polynomial at CGR points, excluding junction point $\mathcal{R}_0$, as follows

$$\mathcal{A}_{\mathbf{N}}\{\varphi\}(r) = \begin{cases} \mathcal{A}_N\varphi\big(r_1(x)\big) & r = r_1(x) \in \mathcal{D}_1 = (0, \mathcal{R}_0], \\ \mathcal{A}_N\varphi\big(r_2(x)\big), & r = r_2(x) \in \mathcal{D}_2 = [\mathcal{R}_0, \infty), \end{cases} \tag{3.29}$$

with each polynomial defined explicitly as below

$$\begin{cases} \mathcal{A}_N\varphi\big(r_1(x)\big) := \sum_{j=0}^{N-1} \varphi\big(r_1(x_j)\big) l_j(x) + \alpha\, l_N(x), & x = 1 - 2r/\mathcal{R}_0, \\ \mathcal{A}_N\varphi\big(r_2(x)\big) := \sum_{j=0}^{N-1} \varphi\big(r_2(x_j)\big) l_j(x) + \alpha\, l_N(x), & x = 1 - 2\mathcal{R}_0/r, \end{cases} \tag{3.30}$$

where the parameter $\alpha \in \mathbb{C}$ is to be determined later to guarantee the derivative continuity at junction point $\mathcal{R}_0$, that is,

$$\frac{\partial}{\partial r}\mathcal{A}_{\mathbf{N}}\{\varphi\}(\mathcal{R}_0 + 0) = \frac{\partial}{\partial r}\mathcal{A}_{\mathbf{N}}\{\varphi\}(\mathcal{R}_0 - 0).$$

The $\mathbf{C}^0$-continuity condition at $\mathcal{R}_0$ holds true automatically.

After a simple but tedious computation, we obtain an explicit formula for α as follows

$$\begin{aligned} \alpha &= -\frac{\sum_{j=0}^{N-1} \varphi(r_1(x_j))\, l_j'(-1) + \sum_{j=0}^{N-1} \varphi(r_2(x_j))\, l_j'(-1)}{2 l_N'(-1)} \\ &= \varphi(\mathcal{R}_0) - \frac{\partial_x \left(I_N\varphi(r_1(x))\right)\Big|_{x=-1} + \partial_x \left(I_N\varphi(r_2(x))\right)\Big|_{x=-1}}{2\, l_N'(-1)}, \\ &:= \varphi(\mathcal{R}_0) - \frac{\beta_1 + \beta_2}{2\, l_N'(-1)}, \end{aligned} \tag{3.31}$$

where $I_N\varphi(r_1(x))$ and $I_N\varphi(r_2(x))$ are the classical Chebyshev-Radau interpolation polynomial as shown in C^0 piecewise interpolation (3.26). Here $\beta_1 = \partial_x(I_N\varphi(r_1))|_{x=-1}$ and $\beta_2 = \partial_x(I_N\varphi(r_2))|_{x=-1}$. Since $I_N\varphi(r_1(x))$ and $I_N\varphi(r_2(x))$ are interpolation polynomials of $\varphi(r_1(x))$ and $\varphi(r_2(x))$, using the standard convergence theory of spectral method [26], the follwoing approximation relations

$$\partial_x\varphi(r_j(x))\Big|_{x=-1} \approx \partial_x(I_N\varphi(r_1))|_{x=-1} = \beta_j, \quad j = 1, 2,$$

holds true and achieves spectral accuracy. Using the relations (3.22)-(3.24) and the chain rule, we have

$$\partial_x\varphi(r_j(x))\Big|_{x=-1} = (-1)^j \frac{\mathcal{R}_0}{2}\, \partial_r\varphi(r)\Big|_{r=\mathcal{R}_0}, \quad j = 1, 2, \tag{3.32}$$

which immediately leads to the following estimation

$$\alpha - \varphi(\mathcal{R}_0) = -(\beta_1 + \beta_2)/(2l'_N(-1)) \approx 0. \tag{3.33}$$

Therefore, we can conclude that the C^1-continuity approximation polynomial is actually a small perturbation of the C^0-continuity interpolation, and it achives the same spectral accuracy. The C^1-continuity polynomial (3.30) can be rewritten as follows

$$\mathcal{A}_N\varphi\big(r_j(x)\big) = I_N\varphi(r_j(x)) - \frac{\beta_1 + \beta_2}{2l'_N(-1)}\; l_N(x), \;\; j = 1, 2. \tag{3.34}$$

The error estimates are summarized in the following theorem, and we choose to present the proof in Appendix Appendix A.

Theorem 2 *Given a function $\varphi(r)$ that is defined on $(0, +\infty)$, if the mapped functions $\varphi(r_1(x)), \varphi(r_2(x)) \in B^m_{-\frac{1}{2},-\frac{1}{2}}([-1, 1])$ and their derivative functions $\partial_x\varphi(r_1(x)), \partial_x\varphi(r_2(x)) \in B^{m-1}_{-\frac{1}{2},-\frac{1}{2}}([-1, 1])$, we have*

$$\|\varphi - \mathcal{A}_{\mathbf{N}}\{\varphi\}\|_\omega \lesssim N^{1-m}, \tag{3.35}$$

where $\|\cdot\|_\omega$ represents the weighted L_2 norm and the weight function $\omega(r)$ is the same as that in Theorem (1).

Remark 3.1 For sake of notational simplicity, here we assume the same degrees of freedom N in both $\mathcal{D}_1$ and $\mathcal{D}_2$ as stated in Theorem 1-2, i.e., $\mathbf{N} = (N, N)$. While, in numerical practice, we can choose different values of N_1 and N_2 so to accommodate its distinct behaviors in each domain.

3.3 Multidomain Chebyshev Spectral Collocation Method

We choose to discretize the spatial operator $\mathcal{L}_k$ (defined in (2.16)) on Chebyshev-Gauss-Radau points using the C^0/C^1-continuity multidomain approximation. Denote by vector

$$\boldsymbol{r}_1^{(0)} = \big[r_1(x_0)\; r_1(x_1)\; \ldots\; r_1(x_N)\big]^T, \quad \boldsymbol{r}_2^{(0)} = \big[r_2(x_N)\; r_2(x_{N-1})\; \ldots\; r_2(x_0)\big]^T,$$
$$\boldsymbol{r}^{(0)} = \big[r_1(x_0)\; \ldots\; r_1(x_N)\; r_2(x_{N-1})\; \ldots\; r_2(x_0)\big]^T,$$

we first discuss the first-order differential operator discretization for C^0 interpolation. For $r \in (0, \mathcal{R}_0]$, we can approximate the derivative of $\varphi(r)$ by the derivatives of its C^0-continuity interpolation (3.26) as

$$\frac{\partial}{\partial r} I_{\mathbf{N}}\{\varphi\}(r_1) = -\frac{2}{\mathcal{R}_0} \sum_{j=0}^{N} \varphi\big(r_1(x_j)\big) l_j'(x).$$

Then, the first-order derivatives, written in matrix form, read as follows

$$\frac{\partial}{\partial r} I_{\mathbf{N}}\{\varphi\}\left(\boldsymbol{r}_{\mathbf{1}}^{(\mathbf{0})}\right) = \boldsymbol{A}\ \varphi\left(\boldsymbol{r}_{\mathbf{1}}^{(\mathbf{0})}\right), \quad a_{kj} = -2l_j'(x_k)/\mathcal{R}_0, \quad 0 \le k, j \le N,$$

where matrix $\boldsymbol{A} \in \mathbb{R}^{(N+1)\times(N+1)}$. While, for $r \in [\mathcal{R}_0, \infty)$, we approximate $\partial_r \varphi(r)$ as

$$\frac{\partial}{\partial r} I_{\mathbf{N}}\{\varphi\}(r_2) = \frac{2\mathcal{R}_0}{r^2} \sum_{j=0}^{N} \varphi\big(r_2(x_j)\big) l_j'(x),$$

and obtain the derivatives in matrix form

$$\frac{\partial}{\partial r} I_{\mathbf{N}}\{\varphi\}\left(\boldsymbol{r}_{\mathbf{2}}^{(\mathbf{0})}\right) = \boldsymbol{F}\ \varphi\left(\boldsymbol{r}_{\mathbf{2}}^{(\mathbf{0})}\right), \quad f_{kj} = 2\mathcal{R}_0 l_{N-j}'(x_{N-k})/r_2^2(x_{N-k}), \quad 0 \le k, j \le N,$$

where matrix $\boldsymbol{F} \in \mathbb{R}^{(N+1)\times(N+1)}$. Using the fact that $\varphi(r_1)(x_N) = \varphi(r_2)(x_N)$, we obtain the first-order differential matrix $\boldsymbol{D}_{\mathbf{1}}^{(\mathbf{0})} \in \mathbb{R}^{(2N+1)\times(2N+1)}$ in the semi-infinite interval as

$$\frac{\partial}{\partial r} I_{\mathbf{N}}\{\varphi\}\left(\boldsymbol{r}^{(\mathbf{0})}\right) = \boldsymbol{D}_{\mathbf{1}}^{(\mathbf{0})} \varphi\left(\boldsymbol{r}^{(\mathbf{0})}\right), \quad \boldsymbol{D}_{\mathbf{1}}^{(\mathbf{0})} = \begin{pmatrix} \boldsymbol{A} & \mathbf{0}_{(\mathrm{N+1})\times \mathrm{N}} \\ \big[\mathbf{0}_{\mathrm{N}\times\mathrm{N}},\ \boldsymbol{F}[2{:}\mathrm{N+1},1]\big] & \boldsymbol{F}[2{:}\mathrm{N+1},2{:}\mathrm{N+1}] \end{pmatrix},$$

where $\mathbf{0}_{m\times n}$ represents the zero matrix of size $m \times n$.

Now we turn to the C^1-continuity approximation case. Define vectors

$$\boldsymbol{r}_{\mathbf{1}}^{(\mathbf{1})} = \big[r_1(x_0)\ \ldots\ r_1(x_{N-1})\big]^T,\ \boldsymbol{r}_{\mathbf{2}}^{(\mathbf{1})} = \big[r_2(x_{N-1})\ \ldots\ r_2(x_0)\big]^T,\ \boldsymbol{r}^{(\mathbf{1})} = \big[\boldsymbol{r}_{\mathbf{1}}^{(\mathbf{1})};\ \boldsymbol{r}_{\mathbf{2}}^{(\mathbf{1})}\big].$$

For $r \in (0, \mathcal{R}_0]$, by taking derivative of the C^1 approximation (3.30), we have

$$\frac{\partial}{\partial r} \mathcal{A}_{\mathbf{N}}\{\varphi\}(r_1) = \frac{-2}{\mathcal{R}_0} \left(\sum_{j=0}^{N-1} \varphi\big(r_1(x_j)\big) \left[l_j'(x) - \frac{l_j'(-1) l_N'(x)}{2 l_N'(-1)} \right] - \sum_{j=0}^{N-1} \varphi(r_2(x_j)) \frac{l_j'(-1) l_N'(x)}{2 l_N'(-1)} \right).$$

We can rewrite it in the following matrix form

$$\frac{\partial}{\partial r} \mathcal{A}_{\mathbf{N}}\{\varphi\}\left(\boldsymbol{r}_{\mathbf{1}}^{(\mathbf{1})}\right) = \boldsymbol{B}\ \varphi\left(\boldsymbol{r}_{\mathbf{1}}^{(\mathbf{1})}\right) + \boldsymbol{C}\ \varphi\left(\boldsymbol{r}_{\mathbf{2}}^{(\mathbf{1})}\right),$$

where matrices $\boldsymbol{B}, \boldsymbol{C} \in \mathbb{R}^{N\times N}$ are given explicitly as

$$b_{kj} = -\frac{2}{\mathcal{R}_0} \left[l_j'(x_k) - \frac{l_j'(-1) l_N'(x_k)}{2 l_N'(-1)} \right],\ c_{kj} = \frac{l_{N-1-j}'(-1) l_N'(x_k)}{\mathcal{R}_0 l_N'(-1)},\ 0 \le k, j \le N-1.$$

For $r \in [\mathcal{R}_0, \infty)$, we approximate $\partial_r \varphi(r)$ as

$$\frac{\partial}{\partial r} \mathcal{A}_{\mathbf{N}}\{\varphi\}(r_2) = \frac{2\mathcal{R}_0}{r^2} \left(\sum_{j=0}^{N-1} \varphi\big(r_2(x_j)\big) \left[l_j'(x) - \frac{l_j'(-1) l_N'(x)}{2 l_N'(-1)} \right] - \sum_{j=0}^{N-1} \varphi\big(r_1(x_j)\big) \frac{l_j'(-1) l_N'(x)}{2 l_N'(-1)} \right),$$

Fig. 2 Error curves

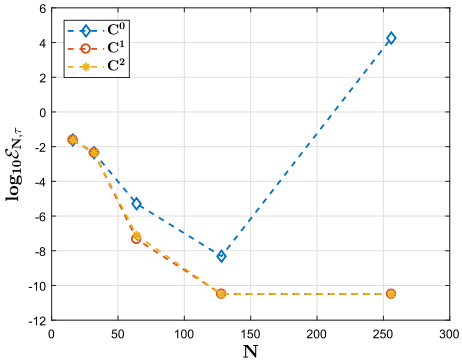

which is rewritten in matrix form as follows

$$\frac{\partial}{\partial r}\mathcal{A}_{\mathbf{N}}\{\varphi\}\left(\boldsymbol{r}_{\mathbf{2}}^{(\mathbf{1})}\right)=\boldsymbol{G}\,\varphi\left(\boldsymbol{r}_{\mathbf{2}}^{(\mathbf{1})}\right)+\boldsymbol{H}\,\varphi\left(\boldsymbol{r}_{\mathbf{1}}^{(\mathbf{1})}\right), \tag{3.36}$$

where matrices $\boldsymbol{G}, \boldsymbol{H} \in \mathbb{R}^{N\times N}$ are given explicitly as

$$g_{kj}=\frac{2\mathcal{R}_0}{r_2^2(x_{N-1-k})}\left[l'_{N-1-j}(x_{N-1-k})-\frac{l'_{N-1-j}(-1)l'_N(x_{N-1-k})}{2l'_N(-1)}\right],$$
$$h_{kj}=-\frac{\mathcal{R}_0 l'_j(-1)l'_N(x_{N-1-k})}{r_2^2(x_{N-1-k})l'_N(-1)},\quad 0\le k,j\le N-1.$$

The first-order differential matrix $\boldsymbol{D}_{\mathbf{1}}^{(\mathbf{1})}\in\mathbb{R}^{2N\times 2N}$ reads explicitly as

$$\frac{\partial}{\partial r}\mathcal{A}_{\mathbf{N}}\{\varphi\}\left(\boldsymbol{r}^{(\mathbf{1})}\right)=\boldsymbol{D}_{\mathbf{1}}^{(\mathbf{1})}\varphi\left(\boldsymbol{r}^{(\mathbf{1})}\right),\quad \boldsymbol{D}_{\mathbf{1}}^{(\mathbf{1})}=\begin{pmatrix}\boldsymbol{B} & \boldsymbol{C}\\ \boldsymbol{H} & \boldsymbol{G}\end{pmatrix}.$$

The second-order differential matrices for C^0/C^1 approximation can be derived similarly and are denoted by $\boldsymbol{D}_2^{(0)}/\boldsymbol{D}_2^{(1)}$ respectively. Then, the spatial operator $\mathcal{L}_k$ is discretized as

$$\boldsymbol{L}_k^{(j)}=\boldsymbol{D}_2^{(j)}+\boldsymbol{R}^{-1}\boldsymbol{D}_1^{(j)}-k^2\boldsymbol{R}^{-2},\quad j=0,1, \tag{3.37}$$

where $\boldsymbol{R}=\mathrm{diag}(\boldsymbol{r}^{(j)})$ is diagonal matrix. The full discrete scheme reads as follows

$$(\boldsymbol{E}-\frac{i\tau}{2}\boldsymbol{L}_k^{(j)})\varphi_k(\boldsymbol{r},t_{n+1})=(\boldsymbol{E}+\frac{i\tau}{2}\boldsymbol{L}_k^{(j)})\varphi_k(\boldsymbol{r},t_n), \tag{3.38}$$

where $\boldsymbol{E}$ is identity matrix. It is important to remark that the C^1-continuity matching conditions is optimal in terms of stability and implementation easiness.

3.4 Optimal Matching Conditions: C^1-continuity

In fact, different matching conditions can be imposed so to guarantee the C^0, C^1 or C^2 continuity. We shall identify the optimal matching conditions in terms of stability.

Let us take $k=0$ in (2.15) as an example. The zero-mode problem

$$\begin{cases} i\partial_t\varphi_0(r,t)=-\mathcal{L}_0\varphi_0(r,t), & r\in(0,\infty),\\ \varphi_0(r,0)=e^{-r^2}, \end{cases} \tag{3.39}$$

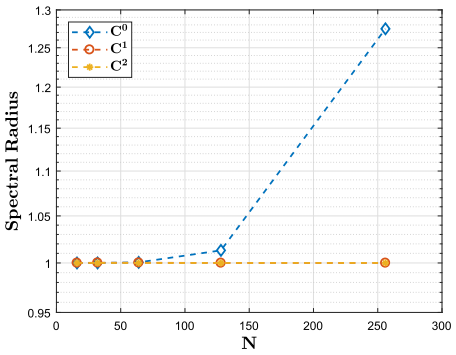

Fig. 3 Spectral radius

admits an exact solution $\varphi_0(r,t) = \frac{i}{i-4t} e^{-\frac{ir^2}{i-4t}}$. In numerical computation, we choose $\mathcal{R}_0 = 10$, time step $\tau = 10^{-5}$ and the final time $T = 10^{-2}$. The numerical solution is denoted by $\varphi_0^{(\mathbf{N},\tau)}$ and its relative error

$$\mathcal{E}_{\mathbf{N},\tau} = \|\varphi_0^{(\mathbf{N},\tau)} - \varphi_0\|_\infty / \|\varphi_0\|_\infty.$$

As illustrated in Figure 2, the multidomain spectral methods imposed with different continuity conditions display similar accuracy for small number of discrete points. However, the numerical errors of C^0 method tends to blow up as N increases, which is attributed to large radius of the corresponding iteration matrix (3.38). In the evolution, round-off errors accumulates and soars to 10^5 with a spectral radius larger than one, which is approximately around 1.28 as shown in Figure 3. While, the C^1 and C^2 methods exhibit similar accuracy and stability. In terms of stability and implementation easiness, the C^1 matching condition is the optimal choice.

We then investigate the accuracy of C^1 method. As stated before, rogue wave solutions may exhibit either fast exponential-decay or slow-decay at the far field. To quantify the comparison, we adopt the following relative error

$$\mathcal{E}_{\mathbf{N}} = \|(\partial_r \mathcal{A}_{\mathbf{N}}\varphi)(R) - (\partial_r \varphi)(R)\|_\infty / \|(\partial_r \varphi)(R)\|_\infty,$$

where $R = (R^{(1)}, R^{(2)})$ is the checkpoint vector with both vectors R^1 and R^2 being constructed with 1000 uniformly distributed points of interval [0, 10] and [10, 100] respectively.

As illustrated in the left side of Figure 4 that: for fast-decay functions, such as $\varphi(r) = e^{-\lambda r}$, and slow-decay functions $\varphi(r) = 1/(1+r)^\beta$ with β not too small, the error curves demonstrate spectral accuracy of the numerical method for both cases. However, for slow-decay case, for instance $\beta = 0.1$, is chosen, it fails to deliver satisfactory accuracy. This can be attributed to the non-differentiability of shifted function $\varphi(r_2(x))$ as stated in the Theorem 2. In the following subsection, we aim to identify a suitable mapping technique that can accommodate the differentiability of such slow-decay functions.

Remark 3.2 While an optimal $\mathcal{R}_0$ values can improve the overall efficiency, we emphasize that the proposed method is robust with respect to $\mathcal{R}_0$ parameter. Indeed, spectral accuracy is achieved for a wide range of $\mathcal{R}_0$ values. Although the required number of points varies slightly, the resulting efficiency variation is minimal. We therefore omit the detailed discussion here.

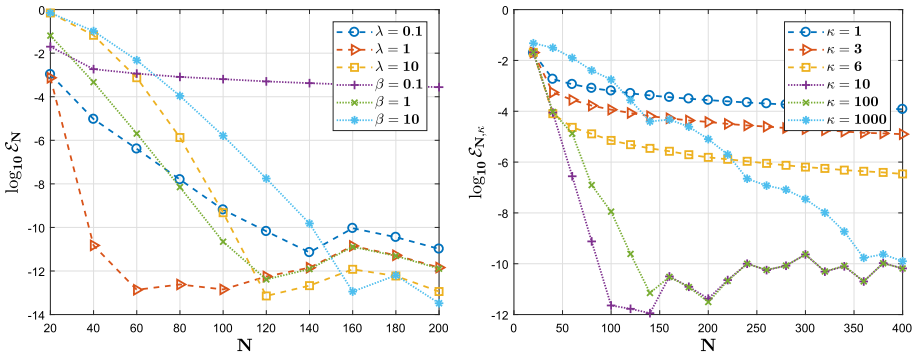

Fig. 4 Convergence curves of C^1 approximation. Left : $e^{-\lambda r}$, $\frac{1}{(1+r)^{\beta}}$. Right : $\frac{1}{(1+r)^{0.1}}$

3.5 High Order Mapping for Slow-Decay Problems

We start with a feasible mapping, which is suitable for a larger class of functions, so to guarantee the continuity/regularity conditions for the mapped function $\varphi(r(x))$. Given a function $\varphi(r)$ and assume the mapping $r(x)$ is monotonic, the first-order derivative of mapped function $\varphi(r(x))$ reads as follows

$$\frac{\partial}{\partial x}\varphi(r(x)) = \frac{\partial \varphi}{\partial r}(r)\cdot\frac{\partial r}{\partial x}(x) = \frac{\varphi'(r)}{x'(r)}, \quad x \in [-1, 1). \tag{3.40}$$

To ensure its continuous differentiability within the closed interval $[-1, 1]$, the term $\varphi'(r)/x'(r)$ should tend to a constant as r approaches infinity, which requires that $x'(r)$ decays slower than $\varphi'(r)$. For this purpose, we modify the first-order mapping (3.24) and introduce the following high-order mapping in Domain II ($\mathcal{D}_2$):

$$\boxed{r^{\kappa}(x) = \frac{2^{\kappa}\mathcal{R}_0}{(1-x)^{\kappa}}, \quad x \in [-1, 1), \quad \kappa \in \mathbb{Z}^+.} \tag{3.41}$$

It is easy to check that a larger mapping order κ implies a higher regularity. While, on the other hand, as depicted in Figure 5, we can see that larger κ increase the sparsity of nodes distribution near the junction in Domain II, thus necessitating more points to guarantee accuracy, which in turn would probabaly reduce the computational efficiency. Therefore, to strike a balance between accuracy and efficiency, we choose the mapping order κ to be slightly larger than the decay rate p, that is

$$\kappa = \lceil\, p^{-1}\,\rceil, \tag{3.42}$$

where the symbol $\lceil\cdot\rceil$ is the rounding up function.

Remark 3.3 For the two-dimensional solutions with an isotropic far-field profile as in (1.2), we can use a uniform mapping parameter κ for all Fourier modes. A straightforward analysis confirms this, showing that all Fourier coefficients $\varphi_k(r)$ share the identical radial decay, upon which the optimal mapping depends.

Now, we can construct the C^1-continuity multidomain spectral approximation using high order mapping similarly as before. We define the high order C^1-continuity multidomain

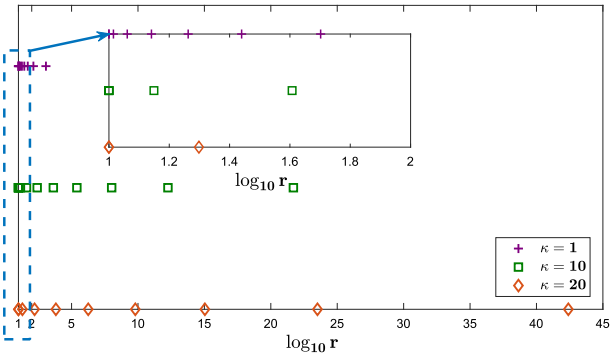

Fig. 5 Distribution of Shifted Chebyshev Gauss-Radau Nodes

approximation

$$\mathcal{A}_{\mathbf{N}}^{\kappa}\{\varphi\}(r)=\begin{cases}\mathcal{A}_N^{\kappa}\varphi\big(r_1(x)\big), & r=r_1(x)=\mathcal{R}_0(1-x)/2 \quad \in(0,\mathcal{R}_0],\\ \mathcal{A}_N^{\kappa}\varphi\big(r^{\kappa}(x)\big), & r=r^{\kappa}(x)=2^{\kappa}\mathcal{R}_0/(1-x)^{\kappa}\in[\mathcal{R}_0,\infty).\end{cases} \tag{3.43}$$

where:

- for $r\in(0,\mathcal{R}_0]$

$$\mathcal{A}_N^{\kappa}\varphi\big(r_1(x)\big)=\sum_{j=0}^{N-1}\varphi\big(r_1(x_j)\big)l_j(x)+\alpha l_N(x),\quad x=1-2r/\mathcal{R}_0,$$

- for $r\in[\mathcal{R}_0,\infty)$

$$\mathcal{A}_N^{\kappa}\varphi\big(r^{\kappa}(x)\big)=\sum_{j=0}^{N-1}\varphi\big(r^{\kappa}(x_j)\big)l_j(x)+\alpha l_N(x),\quad x=1-2\mathcal{R}_0^{1/\kappa}/r^{1/\kappa},$$

the parameter α can be derived using the C^1 matching conditions $\frac{\partial}{\partial_r}[\mathcal{A}_{\mathbf{N}}^{\kappa}\varphi]\big|_{r=\mathcal{R}_0+0}=\frac{\partial}{\partial_r}[\mathcal{A}_{\mathbf{N}}^{\kappa}\varphi]\big|_{\mathcal{R}_0-0}$ as

$$\alpha=-\frac{\kappa\sum_{j=0}^{N-1}\varphi(r_1(x_j))l_j'(-1)+\sum_{j=0}^{N-1}\varphi(r^{\kappa}(x_j))l_j'(-1)}{\kappa l_N'(-1)+l_N'(-1)}. \tag{3.44}$$

After constructing the high order C^1-continuity multidomain spectral approximation, we can discretize the space operator (2.16) similarly. In order to validate the efficiency and accuracy of high order mapping for slow-decay functions, we compare the impacts of different values of κ using the following error

$$\mathcal{E}_{\mathbf{N},\kappa}=\|(\partial_r\mathcal{A}_{\mathbf{N}}^{\kappa}\varphi)(R)-(\partial_r\varphi)(R)\|_{\infty}/\|(\partial_r\varphi)(R)\|_{\infty}.$$

As can be seen from the right side of Figure 4, higher order mapping, e.g., $\kappa\geq 10$, guarantees spectral accuracy for slow-decay functions. Meanwhile, the highest order mapping, namely $\kappa=1000$, requires more dicrete points. In fact, the shifted function $\varphi(r^{\kappa})(x)=1/(1+r^{\kappa}(x))^{0.1}$ is differentiable on the interval $[-1,1]$ for all $\kappa\geq 10$.

Employing the discretization of space operator $\mathcal{L}_k$ (2.16), we can derive the direct full scheme of linear systems (3.38) similarly. Then we could solve the radial problems (2.15) and proceed to simulate the dynamics evolution.

4 Numerical results

Now we are ready to solve the 2D NLSE (1.1). In practice, we allow for different number of discrete points in Domain I and II, and denote them as N_1 and N_2 hereafter. The time step and the final time are denoted by τ and T respectively. The degrees of freedom is denoted by a triple integer-valued vector (M, N_1, N_2), which represents M equidistant points in θ-direction and $(N_1 + N_2 + 1)$ points in r-direction. We shall present extensive numerical results for functions with different decay rates, together with simulation of rogue waves, to confirm the accuracy and efficiency.

Define $\mathcal{S}_m$ as the solver for the systems (3.38), e.g., $\varphi_m(r_k, t_{n+1}) = \mathcal{S}_m(\varphi_m(r_k, t_n))$, we outline the algorithm process for computing 2D dynamics (1.1) in Algorithm 1.

Algorithm 1: Pseudo Codes for NLSE

Input: initial value $\psi_0(\mathbf{x})$, final time T, time step τ, mapping order κ and mesh grid (M, N_1, N_2).
Output: $\psi(\mathbf{x}, T)$.
Initialize $n = 0$, $N_\tau = T/\tau$, the junction point $\mathcal{R}_0 = 10$, discrete vectors R, Θ and the initial wave function $\psi_{kj}^0 = \psi_0(\mathbf{x}_{kj})$.
while $n < N_\tau$ **do**
  $\psi_{kj}^{(1)} \leftarrow e^{-i\mathcal{N}(|\psi_{kj}^n|^2, \mathbf{x}_{kj})\tau/2} \psi_{kj}^n$
  for $m = -\frac{M}{2}$ to $\frac{M}{2} - 1$ **do**
    $\varphi_m(r_k, t_{n+1}) \leftarrow \mathcal{S}_m(\varphi_m(r_k, t_n))$
    $\psi_{kj}^{(2)} \leftarrow \sum_{m=-M/2}^{M/2-1} \varphi_m(r_k, t_{n+1}) e^{ik\theta_j}$
  end for
  $\psi_{kj}^{n+1} \leftarrow e^{-i\mathcal{N}(|\psi_{kj}^{(2)}|^2, \mathbf{x}_{kj})\tau/2} \psi_{kj}^{(2)}$
  $n \leftarrow n + 1$
end while
$\psi(\mathbf{x}_{kj}, T) \leftarrow \psi_{kj}^{N_\tau}$.

To validate our method, we present errors of the numerical solutions at a fixed final time T. To be specific, for equations with analytical solutions, the convergence rate is calculated as

$$\mathcal{E} := \|\psi^{(M,N_1,N_2,\tau,\kappa)} - \psi\|_\infty / \|\psi\|_\infty,$$

where ψ is the exact solution at time T. While, for those without analytical solutions, the self-convergence rates of the spatial discretization, including the radial direction

$$\mathcal{E}^r := \|\psi^{(M,N_1,N_2,\tau,\kappa)} - \psi^{(M,2N_1,2N_2,\tau,\kappa)}\|_\infty / \|\psi^{(M,2N_1,2N_2,\tau,\kappa)}\|_\infty,$$

and the angular direction

$$\mathcal{E}^\theta := \|\psi^{(M,N_1,N_2,\tau,\kappa)} - \psi^{(2M,N_1,N_2,\tau,\kappa)}\|_\infty / \|\psi^{(2M,N_1,N_2,\tau,\kappa)}\|_\infty,$$

are presented. Here $\psi^{(M,N_1,N_2,\tau,\kappa)}$ is the numerical solution with mesh grid (M, N_1, N_2), time step τ and nonlinear mapping order κ.

Example 4.1 (**Convergence test**) Consider the nonlinear term

$$\mathcal{N}(|\psi(\mathbf{x}, t)|^2, \mathbf{x}) = 2\tanh^2 x + 2\tanh^2 y - 3 \tag{4.45}$$

Table 1 Errors in radial and azimuthal directions (Example 4.1)

radial direction				
(N_1, N_2)	(8, 4)	(16, 8)	(32, 16)	(64, 32)
$\mathcal{E}$	6.04E-02	6.23E-04	4.43E-08	6.96E-11
azimuthal direction				
M	32	64	128	256
$\mathcal{E}$	2.93E-04	2.92E-06	3.95E-09	4.84E-11

Table 2 Errors in temporal direction with $\tau_0 = 2 \times 10^{-3}$ (Example 4.1)

τ	τ_0	$\tau_0/2$	$\tau_0/4$	$\tau_0/8$
$\mathcal{E}$	5.09E-07	1.27E-07	3.18E-08	7.96E-09
rate	2	2	2	2
τ	$\tau_0/16$	$\tau_0/32$	$\tau_0/64$	$\tau_0/128$
$\mathcal{E}$	1.99E-09	4.96E-10	1.20E-10	2.86E-11
rate	2	2	2	N/A[1]

The convergence rate is not applicable for the final entry as it is computed from two consecutive errors

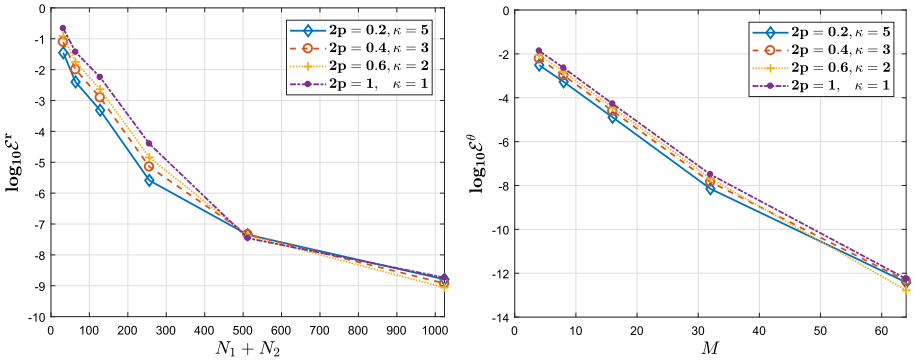

Fig. 6 Radial and azimuthal convergence for different decay rates p and mapping orders κ (Example 4.2)

and the corresponding exact solution

$$\psi(\mathbf{x}, t) = \frac{i \exp it}{\cosh x \cosh y}. \tag{4.46}$$

In order to verify numerical accuracy, we carry out several numerical tests at final time $T = 1$ with mapping order $\kappa = 1$. We first present the spatial accuracy for a very small time step $\tau = 10^{-5}$ in Table 1 with upper part displaying the radial direction accuracy by varying the number of grid points N with a fine mesh in the θ-direction ($M = 256$); and lower part depicting the azimuthal direction accuracy by varying the number of grid points M with a fine mesh in the r-direction ($N_1 = 256, N_2 = 128$). Then, we illustrate the second-order convergence in temporal direction in Table 2 by varying the time step τ while keeping a relatively fine spatial mesh, i.e., $(M, N_1, N_2) = (256, 256, 128)$. From Table 1-2, one can see clearly that our method is spectrally accurate in space and second-order accuracte in time.

Next, we study the slow-decay case by demonstrating the spectral accuracy, which is quantified as the self-convergence rate in spatial directions.

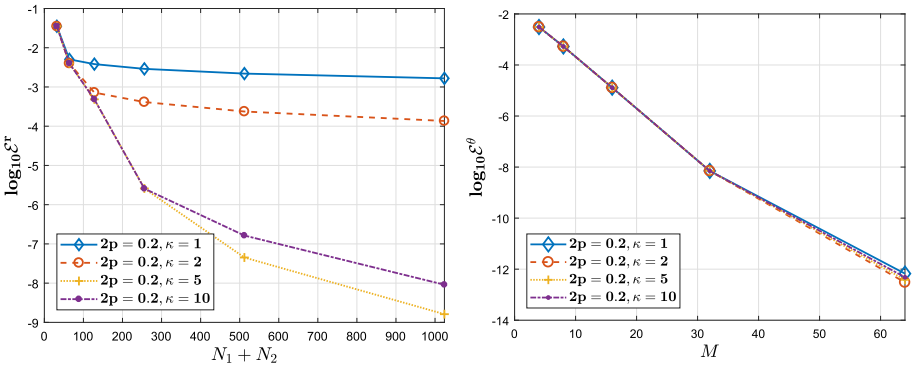

Fig. 7 Radial and azimuthal convergence with fixed decay rate $p = 0.1$ and different mapping orders κ (Example 4.2)

Example 4.2 (**Slow-Decay**) Set the nonlinear term

$$\mathcal{N}(|\psi(\mathbf{x},t)|^2,\mathbf{x}) = |\psi(\mathbf{x},t)|^2 \tag{4.47}$$

and evolve equation (1.1) with initial value

$$\psi_0(x,y) = \frac{1}{(1+2x^2+y^2)^p}, \tag{4.48}$$

where the decay rate is $2p$.

We validate the spatial spectral accuracy by computing self-convergence rates in radial and azimuthal directions at time $T = 0.5$ using a very small time step $\tau = 10^{-4}$ such that errors coming from temporal discretizations are negligible. To show the convergence in radial direction, we choose a fine azimuthal mesh ($M = 64$); while we adopt a very dense radial mesh ($N_2 = 3N_1 = 768$) when investigating the azimuthal convergence. We select suitable mapping orders $\kappa = \lceil 1/2p \rceil$ and plot the the error curves in Figure 6, from which we can observe spectral accuracy in both directions. We then study the necessity of high-order mapping by fixing $2p = 0.2$ and comparing mapping strategies. As shown in the left panel of Figure 7, spectral accuracy in the radial direction is achieved only if $\kappa \geq 1/(2p)$, with the optimal accuracy obtained using mapping strategy (3.41). Notably, all the mapping orders exhibit similar spectral convergence behaviors in the azimuthal direction.

Example 4.3 (**Rogue wave**) We now apply our method to simulate rogue waves. We consider the following nonlinear term

$$\mathcal{N}(|\psi(\mathbf{x},t)|^2,\mathbf{x}) = |\psi(\mathbf{x},t)|^2 + 0.4(x^2+y^2) + 0.26xy \tag{4.49}$$

and the initial value

$$\begin{aligned}\psi_0(x,y) = &\frac{0.1}{1+(x-5)^2+(y-5)^2} + \frac{0.1}{1+(x+5)^2+(y+5)^2} \\ &+ \frac{0.1}{1+(x+5)^2+(y-5)^2} + \frac{0.1}{1+(x-5)^2+(y+5)^2} \\ &+ 0.1\sin(x+y)e^{-0.1x^2-0.1y^2}.\end{aligned} \tag{4.50}$$

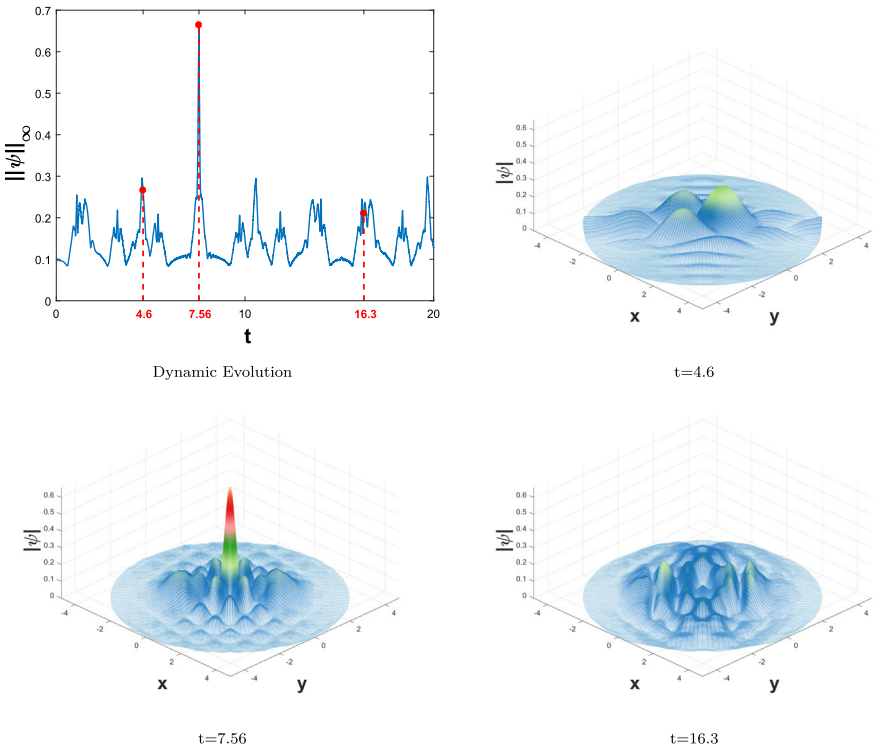

Fig. 8 Rouge wave

The paramters are chosen as: $\mathcal{R}_0 = 10$, $M = 128$, $2N_1 = N_2 = 1024$, $\tau = 10^{-3}$, $\kappa = 5$. We investigate the emergence of rogue waves, as depicted in Figure 8. The wave initiates with a peak height of 0.1 and sustains a consistently low amplitude during its evolution, except at the moment $T = 7.56$ when it exhibits a substantial wave height of 0.66, resembling a snake flicking its red tongue. Following this, we depict snapshots of the wave at various time points in Figure 8, uncovering its notably larger size compared to the population of smaller waves where rogue waves are typically observed.

5 Conclusion

In this article, we propose a time-splitting multidomain Fourier-Chebyshev spectral method to simulate rogue wave by solving a two-dimensional nonlinear Schrödinger equation in the whole space. The Hamiltonian is split into nonlinear part and linear part, and the nonlinear subproblem is integrated exactly in physical space. To solve the linear subproblem efficiently and stably, especially when long term simulation is inevitable, we apply Fourier spectral method in the azimuthal direction and propose the C^1-continuity multidomain Chebyshev spectral method (MCSM) in the radial direction. A nonlinear mapping, along with rigorous analysis, is introduced to deal with the slow-decay case. Extensive numerical results confirm the accuracy and efficiency, and we successfully simulate rogue wave in context of nonlinear Schrödinger equation.

Appendix A. Error Analysis for Multidomain Spectral Method

In this appendix, we shall present the error analysis of C^1-continuity multidomain Chebyshev spectral method. To quantify the error estimate, we define two norms

$$\|\varphi - \mathcal{I}_{\mathbf{N}}\{\varphi\}\|_{\infty,R^+}, \quad \|\varphi - \mathcal{I}_{\mathbf{N}}\{\varphi\}\|_{\omega}, \tag{A.1}$$

where the weight function is defined as

$$\omega(r) = \begin{cases} \frac{1}{\sqrt{r(\mathcal{R}_0 - r)}}, & r \in (0, \mathcal{R}_0], \\ \frac{1}{r\sqrt{r - \mathcal{R}_0}}, & r \in [\mathcal{R}_0, +\infty). \end{cases} \tag{A.2}$$

and $\mathcal{I}_{\mathbf{N}}\{\varphi\}$ is the C^1-continuity multidomain Chebyshev interpolation of $\varphi(r)$.

Theorem 3 *For smooth function $\varphi(r)$ defined on $(0, +\infty)$, let $r_1(x) = \mathcal{R}_0(1-x)/2$ and $r_2(x) = 2\mathcal{R}_0/(1-x)$, we assume the shifted functions $\varphi(r_1)(x)$ and $\varphi(r_2)(x)$ are both analytic in Bernstein ellipse $\mathcal{B}_\rho$ [29] with ± 1 as foci, and $\rho > 1$ as the sum of its semimajor and semiminor:*

$$\mathcal{B}_\rho : \quad z = \frac{1}{2}\left(\rho\, e^{i\theta} + \rho^{-1} e^{-i\theta}\right), \quad 0 \le \theta \le 2\pi,$$

then we have

$$\|\varphi - \mathcal{I}_{\mathbf{N}}\{\varphi\}\|_{\infty,R^+} \lesssim \rho^{-N}. \tag{A.3}$$

Proof We begin with the relation that

$$\|\varphi - \mathcal{I}_{\mathbf{N}}\varphi\|_{\infty,R^+} = \max\left(\|\varphi(r_1) - \mathcal{I}_N\varphi(r_1)\|_{\infty,[-1,1]}, \|\varphi(r_2) - \mathcal{I}_N\varphi(r_2)\|_{\infty,[-1,1]}\right) \tag{A.4}$$

Next, we estimate the term $\|\varphi(r_1) - \mathcal{I}_N\varphi(r_1)\|_{\infty,[-1,1]}$ as an example, while another term can be analysed similarly. Via triangle inequality, we obtain

$$\|\varphi(r_1) - \mathcal{I}_N\varphi(r_1)\|_\infty \le \|\varphi(r_1) - I_N\varphi(r_1)\|_\infty + \|I_N\varphi(r_1) - \mathcal{I}_N\varphi(r_1)\|_\infty. \tag{A.5}$$

According to error estimates of Chebyshev spectral method in [36], the first part can be estimated as follows:

$$\|\varphi(r_1) - I_N\varphi(r_1)\|_\infty \lesssim \rho^{-N}. \tag{A.6}$$

While for the second part, note that the expression of α (3.31) and the matching conditions

$$\varphi(r_1)'(-1) + \varphi(r_2)'(-1) = 0, \tag{A.7}$$

we have

$$\begin{aligned} \| & I_N\varphi(r_1) - \mathcal{I}_N\varphi(r_1)\|_\infty \\ &= \| \frac{[I_N\varphi(r_1(x)) + I_N\varphi(r_2(x))]'\big|_{x=-1}}{2l_N'(-1)} l_N(x)\|_\infty \\ &\lesssim N^{-2}\left(|I_N'\varphi(r_1)(-1) - \varphi(r_1)'(-1)| + |I_N'\varphi(r_2)(-1) - \varphi(r_2)'(-1)|\right) \\ &\lesssim \frac{\rho^{-N}}{N}. \end{aligned}$$

Combining the two results, the first part can be estimated as follows:

$$\|\varphi(r_1) - \mathcal{I}_N\varphi(r_1)\|_{\infty,[-1,1]} \lesssim \rho^{-N}. \tag{A.8}$$

For the second part, we can derive the same result. Finally, the proof is finished. □

Remark Appendix A.1. *In fact,* $\varphi(r) = \frac{P_m(r)}{P_n(r)}, r \in (0, +\infty)$ *statisfies the conditions above as long as* $n \geq m$ *and* $P_n(x)$ *has no zeros on the positive real axis. Here,* $P_n(x)$ *represents the polynomial of degree n.*

Lemma 1 *For function* $f \in B^m_{-1/2,-1/2}(I)$ *and* $f' \in B^{m-1}_{-1/2,-1/2}(I)$*, we have the following estimate*

$$|f'(-1) - I'_N(f)(-1)| \lesssim N^{3-m}, \tag{A.9}$$

where $B^m_{-1/2,-1/2}(I)$ *represents the non-uniformly Jacobo-weighted Sobolev space [26] and* I *represents the interval* $[-1, 1]$.

Proof By applying Rolle's theorem, it can be concluded that since $I_N f - f$ equals to zero at certain specific points, there must exist a constant $\xi \in (-1, 1)$ that satisfies the relation $I'_N f(\xi) - f'(\xi) = 0$. Thus, the estimand can be rewritten using Cauchy-Schwartz inequality

$$\begin{aligned} |f'(-1) - I'_N(f)(-1)| &= |\int_{-1}^{\xi} \left(f'' - I''_N f\right) dx| \\ &\leq \int_{-1}^{1} |f'' - I''_N(f)|(1-x^2)^{1/4}(1-x^2)^{-1/4} dx \\ &\leq \sqrt{\pi} \|f'' - I''_N(f)\|_{\omega^{1/2,1/2}}, \end{aligned}$$

where $\|\cdot\|_{\omega^{\alpha,\beta}}$ represents the weighted L_2 norm with weighted function $\omega^{\alpha,\beta} = (1-x)^\alpha (1+x)^\beta$. By introducing orthogonal projection approximation $\pi_N^{\alpha,\beta}$ [26], we obtain

$$\|f'' - I''_N f\|_{\omega^{\frac{1}{2},\frac{1}{2}}} \leq \|\partial_x \left(f' - \pi_{N-1}^{-\frac{1}{2},-\frac{1}{2}}(f')\right)\|_{\omega^{\frac{1}{2},\frac{1}{2}}} + \|\partial_x \left(\pi_{N-1}^{-\frac{1}{2},-\frac{1}{2}}(f') - I'_N(f)\right)\|_{\omega^{\frac{1}{2},\frac{1}{2}}}$$

We define the first estimand as E_1 and the second estimand as E_2. Employing the error estimate of Chebyshev projection approximation for E_1 [26], we acquire the estimate that

$$E_1 \lesssim N^{2-m} \|\partial_x^m f\|_{\omega^{m-3/2,m-3/2}}, \tag{A.10}$$

when $m = o(N)$. For the estimand E_2, we utilize the inverse formula and get the error estimate as follows

$$\begin{aligned} E_2 &\lesssim (N-1)^2 \|\pi_{N-1}^{-1/2,-1/2}(f') - I'_N(f)\|_{\omega^{1/2,1/2}} \\ &\leq (N-1)^2 \left(\|\pi_{N-1}^{-1/2,-1/2}(f') - f'\|_{\omega^{-1/2,-1/2}} + \|f' - I'_N(f)\|_{\omega^{1/2,1/2}}\right) \\ &\lesssim N^2 \left(N^{1-m} \|\partial_x^m f\|_{\omega^{m-3/2,m-3/2}} + N^{1-m} \|\partial_x^m f\|_{\omega^{m-1/2,m-1/2}}\right) \lesssim N^{3-m}. \end{aligned}$$

Combining the error estimate for estimand E_1 and E_2, we obtain the final result. □

Theorem 4 *For function $\varphi(r)$ defined on $(0, +\infty)$, if functions $\varphi(r_1)(x), \varphi(r_2)(x) \in B^m_{-\frac{1}{2},-\frac{1}{2}}([-1,1])$ and $\varphi(r_1)'(x), \varphi(r_2)'(x) \in B^{m-1}_{-\frac{1}{2},-\frac{1}{2}}([-1,1])$, where $r_1(x) = \mathcal{R}_0(1-x)/2$ and $r_2(x) = 2\mathcal{R}_0/(1-x)$. We have that*

$$\|\varphi - \mathcal{I}_{\mathbf{N}}\{\varphi\}\|_\omega \lesssim N^{1-m}, \tag{A.11}$$

where $\mathbf{N} = (N, N)$ and $\|\cdot\|_\omega$ represents the weighted L_2 norm with

$$\omega(r) = \begin{cases} \frac{1}{\sqrt{r(\mathcal{R}_0 - r)}}, & r \in (0, \mathcal{R}_0], \\ \frac{1}{r\sqrt{r - \mathcal{R}_0}}, & r \in [\mathcal{R}_0, +\infty). \end{cases} \tag{A.12}$$

Proof Via triangular inequality, we have

$$\|\varphi - \mathcal{I}_{\mathbf{N}}\{\varphi\}\|_\omega \le \|\varphi - I_{\mathbf{N}}\{\varphi\}\|_w + \|I_{\mathbf{N}}\{\varphi\} - \mathcal{I}_{\mathbf{N}}\{\varphi\}\|_\omega, \tag{A.13}$$

where the first part can be bounded by N^{-m} according to Theorem 1. For the second norm, via the triangle inequality and the chain rule, we obtain

$$\begin{aligned} \|I_{\mathbf{N}}\{\varphi\} - \mathcal{I}_{\mathbf{N}}\{\varphi\}\|_\omega &\lesssim \|(\alpha - \varphi(\mathcal{R}_0))l_N(x)\|_{\omega^{-\frac{1}{2},-\frac{1}{2}}} \\ &\lesssim \|\frac{[I_N\varphi(r_1(x)) + I_N\varphi(r_2(x))]'\big|_{x=-1}}{2l_N'(-1)}\|_{\omega^{-\frac{1}{2},-\frac{1}{2}}}. \end{aligned} \tag{A.14}$$

Using Lemma 1, we can finally obtain

$$\|I_{\mathbf{N}}\{\varphi\} - \mathcal{I}_{\mathbf{N}}\{\varphi\}\|_\omega \lesssim N^{1-m}. \tag{A.15}$$

Combining the two results, we can prove the theorem. □

Funding S. Chen was supported by the National Natural Science Foundation of China (No. 12471341). G. Liu was supported by the National Natural Science Foundation of China (W2431008). Z. Xu was supported by the National Natural Science Foundation of China (No. 12271400). Y. Zhang was supported by the National Key R&D Program of China (No. 2024YFA1012803), basic research fund of Tianjin University (2025XJ21-0010), and the National Natural Science Foundation of China (No. 12271400).

Data Availability Data sharing is not applicable to this article as no datasets were generated or analyzed.

Declarations

conflict of intrest None

References

1. Akhmediev, N., Ankiewicz, A., Soto-Crespo, J.M.: Rogue waves and rational solutions of the nonlinear Schrödinger equation, Phys. Rev. E, **80**, article 026601 (2009)
2. Akhmediev, N., Dudley, J.M., Solli, D.R., Turitsyn, S.K.: Recent progress in investigating optical rogue waves, J. Opt., **15**, article 060201 (2013)
3. Antoine, X., Arnold, A., Besse, C., Ehrhardt, M., Schädle, A.: A review of transparent and artificial boundary conditions techniques for linear and nonlinear schrödinger equations, commun. Comput. Phys. **4**, 729–796 (2008)
4. Bao, W., Cai, Y.: Mathematical theory and numerical methods for bose-einstein condensation. Kinet. Relat. Mod. **6**, 1–135 (2013)
5. Bao, W., Tang, Q., Xu, Z.: Numerical methods and comparison for computing dark and bright solitons in the nonlinear schrödinger equation. J. Comput. Phys. **235**, 423–445 (2013)

6. Birem, M., Klein, C.: Multidomain spectral method for schrödinger equations. Adv. Comput. Math. **42**, 395–423 (2016)
7. Chang, Q., Jia, E., Sun, W.: Difference schemes for solving the generalized nonlinear schrödinger equation. J. Comput. Phys. **148**, 397–415 (1999)
8. Chen, S., Shen, J.: Log orthogonal functions in semi-infinite intervals: approximation results and applications. SIAM J. Numer. Anal. **61**, 110–134 (2023)
9. Fan, C., Staffilani, G., Zhao, Z.: On decaying properties of nonlinear schrödinger equations. SIAM J. Math. Anal. **56**, 3082–3109 (2024)
10. Funaro, D., Kavian, O.: Approximation of some diffusion evolution equations in unbounded domains by hermite functions. Math. Comp. **57**, 597–619 (1991)
11. Fotopoulos, G., Karachalios, N.I., Koukouloyannis, V., Vetas, K.: The linearly damped nonlinear schrödinger equation with localized driving: spatiotemporal decay estimates and the emergence of extreme wave events. Z. Angew. Math. Phys. **71**, 1–23 (2019)
12. Ganshin, A.N., Efimov, V.B., Kolmakov, G.V., Mezhov-Deglin, L.P., McClintock, P.V.E.: Observation of an inverse energy cascade in developed acoustic turbulence in superfluid helium, Phys. Rev. Lett., **101**, article 065303 (2008)
13. Guo, B.: Error estimation of hermite spectral method for nonlinear partial differential equations. Math. Comp. **68**, 1067–1078 (1999)
14. Guo, B., Shen, J.: Laguerre-galerkin method for nonlinear partial differential equations on a semi-infinite interval. Numer. Math. **86**, 635–654 (2000)
15. Guo, B., Shen, J., Wang, Z.: A rational approximation and its applications to differential equations on the half line. J. Sci. Comput. **15**, 117–147 (2000)
16. Guo, B., Shen, J., Wang, Z.: Chebyshev rational spectral and pseudospectral methods on a semi?infinite interval. Int. J. Numer. Meth. Eng. **53**, 65–84 (2002)
17. Guo, B., Shen, J., Xu, C.: Spectral and pseudospectral approximations using hermite functions: application to the dirac equation. Adv. Comput. Math. **19**, 35–55 (2003)
18. Guo, B., Wang, T.: Composite laguerre-legendre spectral method for exterior problems. Adv. Comput. Math. **32**, 393–429 (2010)
19. Hu, Z., Zhang, X., Li, Y., Li, X., Qin, H.: Numerical simulations of super rogue waves in a numerical wave tank, Ocean Eng., **229**, article 108929 (2021)
20. Kharif, C., Pelinovsky, E.: Physical mechanisms of the rogue wave phenomenon. Eur. J. Mech. B/Fluids **22**, 603–634 (2003)
21. Li, S., Prinari, B., Biondini, G.: Solitons and rogue waves in spinor Bose-Einstein condensates, Phys. Rev. E, **97**, article 022221 (2018)
22. Liu, L., Sun, W., Malomed, B.A.: Formation of rogue waves and modulational instability with zero-wavenumber gain in multicomponent systems with coherent coupling, Phys. Rev. Lett., **131**, article 093801 (2023)
23. Müller, P., Garrett, C., Osborne, A.: Rogue waves. Oceanogr. **18**, 66–75 (2005)
24. Onorato, M., Residori, S., Bortolozzo, U., Montina, A., Arecchi, F.T.: Rogue waves and their generating mechanisms in different physical contexts. Phys. Rep. **528**, 47–89 (2013)
25. Peregrine, D.H.: Water waves, nonlinear schrödinger equations and their solutions. J. Austral. Math. Soc. Ser. B **25**, 16–43 (1983)
26. Shen, J., Tang, T., Wang, L.: Spectral methods: algorithms, analysis and applications, Springer, **41** (2011)
27. Shen, J., Wang, L.: Some recent advances on spectral methods for unbounded domains, commun. Comput. Phys. **5**, 195–241 (2009)
28. Solli, D.R., Ropers, C., Koonath, P., Jalali, B.: Optical rogue waves. Nature **450**, 1054–1057 (2007)
29. Trefethen, L.N.: Approximation theory and approximation practice, extended edition, SIAM, (2019)
30. Wang, H.: An efficient chebyshev-tau spectral method for ginzburg–landau–schrödinger equations. Comput. Phys. Commun. **181**, 325–340 (2010)
31. Wang, H., Wang, J., Zhang, S., Zhang, Y.: A time splitting Chebyshev-Fourier spectral method for the time-dependent rotating nonlocal Schrödinger equation in polar coordinates, J. Comput. Phys., **498**, article 112680 (2014)
32. Wang, P., Xu, Z., Yin, J.: Simple high-order boundary conditions for computing rogue waves in the nonlinear Schrödinger equation, Comput. Phys. Commun., **251**, article 107109 (2020)
33. Wang, R., Ling, L., Zeng, D., Feng, B.: A deep learning improved numerical method for the simulation of rogue waves of nonlinear Schrödinger equation, Commun. Nonlinear Sci. Numer. Simul., **101**, article 105896 (2021)
34. Weideman, J., Herbst, B.: Split-step methods for the solution of the nonlinear schrödinger equation. SIAM J. Numer. Anal. **23**, 485–507 (1986)
35. Yan, Z.: Financial rogue waves. Commun. Theor. Phys. **54**, 947–949 (2010)

36. Zhang, Z.: Superconvergence points of polynomial spectral interpolation. SIAM J. Numer. Anal. **50**, 2966–2985 (2012)